nature structural & molecular biology

Syntaxin opening by the MUN domain underlies the function of Munc13 in synaptic-vesicle priming

Xiaoyu Yang[1,7], Shen Wang[1,7], Yi Sheng[1,7], Mingshu Zhang[2], Wenjuan Zou[3], Lijie Wu[4], Lijun Kang[3], Josep Rizo[5], Rongguang Zhang[2,4], Tao Xu[1,2,6] & Cong Ma[1]

UNC-13-Munc13s have a central function in synaptic-vesicle priming through their MUN domains. However, it is unclear whether this function arises from the ability of the MUN domain to mediate the transition from the Munc18-1–closed syntaxin-1 complex to the SNARE complex *in vitro*. The crystal structure of the rat Munc13-1 MUN domain now reveals an elongated, arch-shaped architecture formed by α-helical bundles, with a highly conserved hydrophobic pocket in the middle. Mutation of two residues (NF) in this pocket abolishes the stimulation caused by the Munc13-1 MUN domain on SNARE-complex assembly and on SNARE-dependent proteoliposome fusion *in vitro*. Moreover, the same mutation in UNC-13 abrogates synaptic-vesicle priming in *Caenorhabditis elegans* neuromuscular junctions. These results support the notion that orchestration of syntaxin-1 opening and SNARE-complex assembly underlies the central role of UNC-13-Munc13s in synaptic-vesicle priming.

Neurotransmitter release mediated by Ca^{2+}-triggered synaptic-vesicle exocytosis is a fundamental process for synaptic transmission. This process is tightly regulated by multiple proteins that form the release machinery. The core machinery includes the neuronal SNAREs syntaxin-1, SNAP-25 and synaptobrevin, as well as the Sec1-Munc18 protein Munc18-1 (refs. 1–4). These proteins are conserved in eukaryotes including yeast and humans, and they have key functions in most types of intracellular membrane fusion. The SNAREs play a central part in membrane fusion by forming tight SNARE complexes through their SNARE motifs, to force the vesicle and plasma membranes into proximity[5–8]. Munc18-1 orchestrates SNARE-complex assembly through its interactions with the SNAREs. For instance, Munc18-1 locks syntaxin-1 in a closed conformation that involves intramolecular binding of syntaxin-1's N-terminal H_{abc} domain and SNARE motif, thus gating entry of syntaxin-1 into the SNARE complex[9–11]. Munc18-1 also interacts with an N-terminal sequence of syntaxin-1 called the N peptide and with the assembled SNARE complex containing an open conformation of syntaxin-1, both of which have been suggested to help to catalyze membrane fusion[12–14]. These multiple interactions, which coordinate syntaxin-1 opening and SNARE-complex assembly, are believed to be spatially and temporally modulated by other key proteins to enable the exquisite regulation of neurotransmitter release.

Particularly important among these proteins are the UNC-13-Munc13s, which are large (~200-kDa) multidomain proteins from presynaptic active zones where vesicles are released[15]. Physiological data have shown that UNC-13-Munc13s are crucial components of the release machinery, because release is totally abolished in neurons lacking these proteins, and that UNC-13-Munc13s play a central part in synaptic-vesicle priming[16–19]. This function relies on an autonomously folded C-terminal region of UNC-13-Munc13s called the MUN domain (**Fig. 1**), which is regarded as the minimal module required for the crucial vesicle-priming function of UNC-13-Munc13s (refs. 20–22). The finding that syntaxin-1 bearing a so-called 'LE mutation' that facilitates opening of syntaxin-1 partially rescues release in *C. elegans* deficient in *unc-13* suggested that UNC-13-Munc13s are involved in opening syntaxin-1 (ref. 23). However, it was unclear whether direct physical interactions between UNC-13-Munc13s and the SNAREs or Munc18-1 underlie this function. For instance, the syntaxin-1 LE mutant also rescued the phenotype observed in the absence of Unc10-RIMs[24], which are active zone proteins with functions that are coupled to UNC-13-Munc13s[1]. A direct role for the UNC-13-Munc13s in opening syntaxin-1 was strongly supported by recent *in vitro* studies showing that the Munc13-1 MUN domain accelerates the transition from the Munc18-1–closed syntaxin-1 complex to the SNARE complex[15] and stimulates SNARE-mediated liposome fusion[25]. However, the biological relevance of these findings has not been tested with physiological experiments *in vivo*.

Sequence analyses have indicated that the UNC-13-Munc13 MUN domain is homologous to subunits from diverse tethering factors involved in traffic at multiple membrane compartments, such as the exocyst, GARP, COG and Dsl1p complexes[26]. This homology and the crystal structures available for some of these tethering factors[27],

[1]Key Laboratory of Molecular Biophysics of the Ministry of Education, College of Life Science and Technology, Huazhong University of Science and Technology, Wuhan, China. [2]National Laboratory of Biomacromolecules, Institute of Biophysics, Chinese Academy of Sciences, Beijing, China. [3]Institute of Neuroscience, Zhejiang University, Hangzhou, China. [4]Institute of Biochemistry and Cell Biology, Shanghai Institutes for Biological Sciences, Chinese Academy of Sciences, Shanghai, China. [5]Department of Biophysics, Biochemistry and Pharmacology, University of Texas Southwestern Medical Center, Dallas, Texas, USA. [6]College of Life Sciences, University of Chinese Academy of Sciences, Beijing, China. [7]These authors contributed equally to this work. Correspondence should be addressed to C.M. (cong.ma@mail.hust.edu.cn) or T.X. (xutao@ibp.ac.cn).

Received 4 January; accepted 1 May; published online 1 June 2015; doi:10.1038/nsmb.3038

particularly that of Sec6p[28], suggested that the UNC-13-Munc13 MUN domain contains four subdomains (termed A–D). Indeed, the crystal structure of the region of the Munc13-1 MUN domain spanning the C and D subdomains (MUN-CD) revealed a striking structural similarity with the tethering factors[29], thus suggesting that UNC-13-Munc13s might play a part in vesicle tethering through the MUN domain in addition to functioning in synaptic-vesicle priming. However, to our knowledge, no three-dimensional structure of an entire UNC-13-Munc13 MUN domain has been described, and this has hindered studies involving structure-activity relationships to test the biological relevance of the activity of the MUN domain in opening syntaxin-1 *in vitro* or of its putative function in tethering. Moreover, the structure of the UNC-13-Munc13 MUN domain is the only one lacking for a central component of the neurotransmitter-release machinery, because structures have been described for other key components such as the three neuronal SNAREs, Sec1-Munc18s, syntaptotagmin-1 and complexins (reviewed in ref. 30).

To shed light on the way in which UNC-13-Munc13s regulate syntaxin-1 opening and vesicle priming, we have determined the crystal structure of the Munc13-1 MUN domain at 2.9-Å resolution. Using *in vitro* fluorescence resonance energy transfer (FRET) and reconstitution experiments, we have identified two highly conserved residues located in the middle of the MUN domain as key sites that mediate opening of syntaxin-1 and SNARE-complex assembly. Furthermore, electrophysiological data recorded at cholinergic neuromuscular junctions (NMJs) of *C. elegans* confirm that these two residues are important for both spontaneous and evoked neurotransmitter release, thus reflecting a critical role in vesicle priming. These results provide compelling evidence that the activity of the MUN domain in stimulating the transition from the Munc18-1–closed syntaxin-1 complex to the SNARE complex *in vitro* underlies the crucial function of UNC-13-Munc13s in synaptic-vesicle priming *in vivo*.

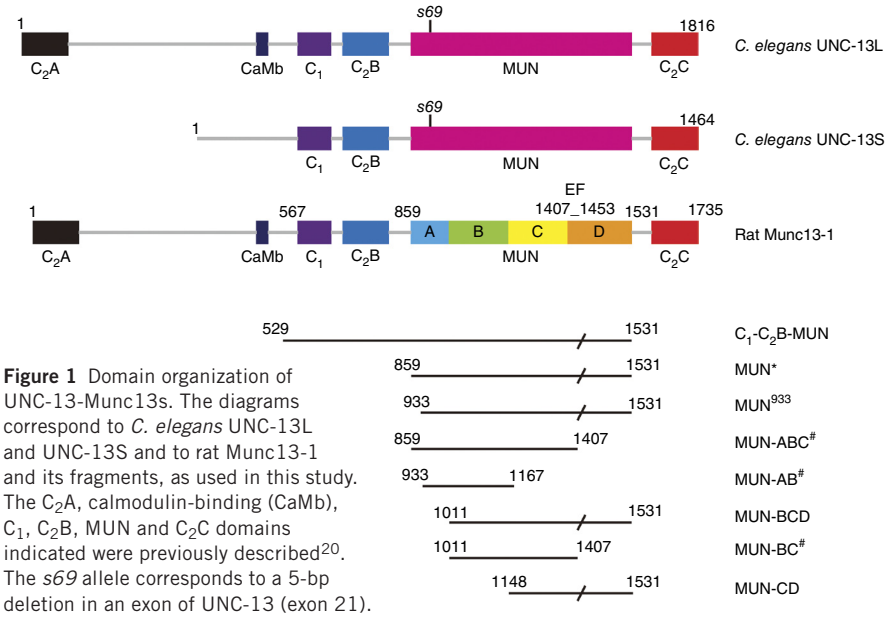

Figure 1 Domain organization of UNC-13-Munc13s. The diagrams correspond to *C. elegans* UNC-13L and UNC-13S and to rat Munc13-1 and its fragments, as used in this study. The C_2A, calmodulin-binding (CaMb), C_1, C_2B, MUN and C_2C domains indicated were previously described[20]. The *s69* allele corresponds to a 5-bp deletion in an exon of UNC-13 (exon 21). Residue numbers indicate selected domain and fragment boundaries. The predicted subdomains within the MUN domain are colored in blue, green, yellow and orange and are labeled A–D. A long loop of the MUN domain that spans residues 1408–1452 was deleted and replaced with residues glutamate and phenylalanine (EF), represented by a slash. For the proper folding of the fragments indicated by #, the boundaries of subdomains B and C are extended to residues 1167 and 1407, respectively, rather than ending at residues 1148 and 1314, as defined from the structure. All fragments used are well folded according to analyses by CD spectroscopy (**Supplementary Fig. 2a**).

RESULTS

Crystal structure of the Munc13-1 MUN domain

The Munc13-1 MUN domain (residues 859–1531, **Fig. 1**) is regarded as the minimal module required for the activity of Munc13-1 in synaptic-vesicle priming[20]. As mentioned above, structure-based sequence alignments using the available structures of tethering factors homologous to Munc13-1 (ref. 26) have indicated that the MUN domain contains four subdomains termed A–D and have identified a highly conserved sequence on the C-terminal region of the MUN domain (MUN-CD, residues 1148–1531), thus aiding in the elucidation of the crystal structure of the MUN-CD region[29]. However, the ability of MUN-CD to open syntaxin-1 is strongly impaired, consistently with physiological data showing that a fragment (residues 1045–1531) encompassing the MUN-CD region is unable to rescue neurotransmitter release[20]. These data imply that the N-terminal portion of the MUN domain (called MUN-AB, residues 859–1147) is indispensable for the priming activity of the MUN domain. Thus, we aimed to crystallize the entire MUN domain containing its A–D subdomains.

Previously, by removing a flexible loop (residues 1408–1452), we successfully improved the yield and solubility of the MUN domain[15] (referred to as MUN*, residues 859–1407, EF, 1453–1531 (**Fig. 1**)), but we were still not be able to obtain high-quality crystals of MUN* for structure determination. To solve this problem, we designed a series of truncations of MUN* (data not shown). Among these truncations, a fragment lacking the first 74 residues on the N terminus of MUN* (referred to as MUN^{933}, residues 933–1407, EF, 1453–1531, **Fig. 1**) finally crystallized. We determined the MUN^{933} structure and refined it to 2.9 Å in resolution (Online Methods, **Fig. 2a** and **Table 1**), and the crystals contained one molecule per asymmetric unit.

The structure of MUN^{933} exhibits an elongated shape spanning 150 Å in length. Consecutive helices pack against each other in a mixed antiparallel or parallel manner and stabilize the whole structure by interhelical interactions. MUN^{933} is composed of helical-bundle subdomains connected by flexible loops and short turns (**Fig. 2a**). Its four subdomains (A–D) are aligned accordingly from the N to C terminus along the MUN^{933} structure (**Fig. 2a**). Subdomains A–D consist of helices H1 and H2 (A), H3–H6 (B), H7–H11 (C) and H12–H15 (D) (**Fig. 2a**,**b**). H7 forms a long and continuous helix that bends and changes direction gradually, with its N-terminal portion packed against the preceding helix H6. MUN^{933} is considerably charged, with positive and negative charges widely distributed throughout the surface (**Supplementary Fig. 1a**). An exposed hydrophobic patch at the junction of subdomains B and C that involves helices H6, H7 and H8 (**Supplementary Fig. 1b**) is found on the surface of MUN^{933}, as discussed below.

As expected, MUN^{933} has a similar architecture to those of vesicle-tethering factors including Sec6p, Tip20 and Exo70 (refs. 28,31–33) (**Fig. 2c**). However, MUN^{933} adopts a distinctive arch-shaped architecture that differs from the more straight structure of Exo70 and the sharply hooked shape of Tip20. It is unclear whether the overall arch

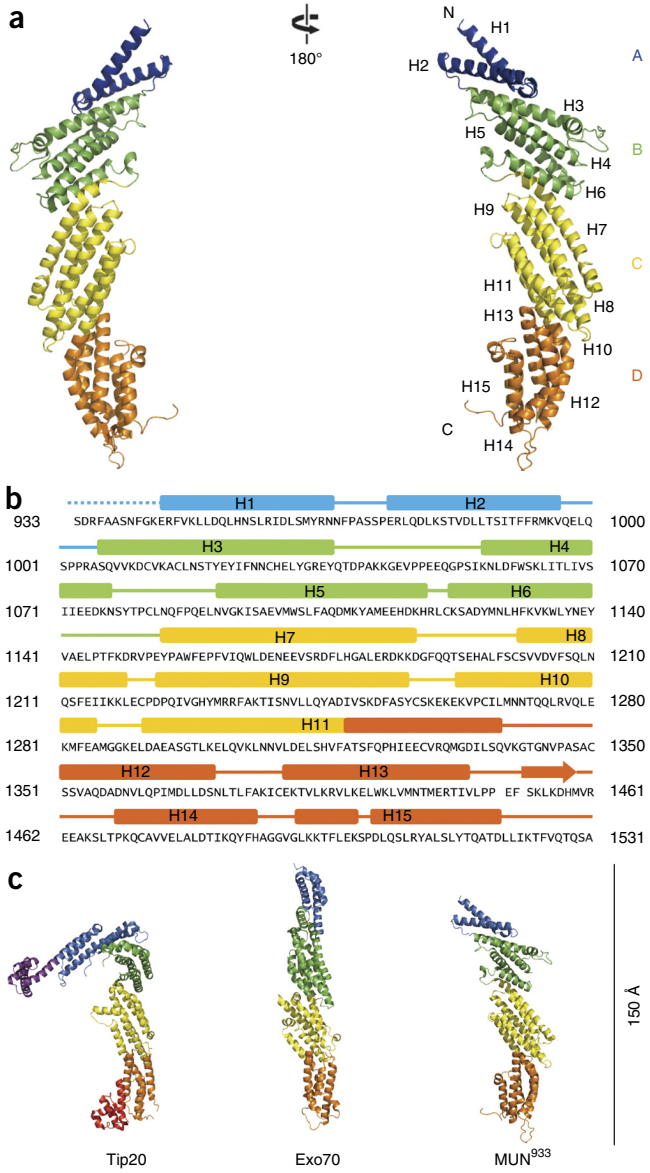

Figure 2 Crystal structure of the Munc13-1 MUN domain. (**a**) Ribbon diagrams of the crystal structure of MUN^{933}, shown in two orientations rotated ~180° with respect to each other. Subdomains A–D are labeled and colored in blue, green, yellow and orange, respectively. Helices H1–H15 are labeled from the N to the C terminus of the structure. (**b**) Sequence of MUN^{933}. Secondary-structure elements are labeled and colored as in **a**. Dotted line represents regions in the crystal structure that are either flexible or disordered. (**c**) Comparison of the structure of MUN^{933} with those of homologous tethering factors that have been solved (Tip20, PDB 3FHN[31]; Exo70, PDB 2PFT[33]).

shape of MUN^{933} may result from crystal packing, but this feature might be important for the functional specificity of the MUN domain in synaptic-vesicle priming.

A conserved hydrophobic pocket is key for opening syntaxin-1

Previous studies have shown that Munc13-1 MUN* stimulates the transition from the Munc18-1–syntaxin-1 complex to the SNARE complex[15]. We thus performed FRET experiments to investigate the activity of MUN^{933} in the stimulation (**Fig. 3a–e**). SNARE-assembly reactions initiated with syntaxin-1 alone or the Munc18-1–syntaxin-1 complex illustrate that Munc18-1 strongly inhibits SNARE-complex formation, whereas addition of either MUN* or MUN^{933} facilitates SNARE-complex assembly equally (**Fig. 3b**). This result confirms that MUN^{933} is functional in stimulating SNARE-complex assembly starting from the Munc18-1–syntaxin-1 complex.

To identify the region of MUN^{933} responsible for this activity, we used the solved structure of MUN^{933} as a guide and designed several fragments that encompass one or more subdomains of MUN^{933}, referred to as MUN-ABC, MUN-BCD, MUN-AB, MUN-BC and MUN-CD (**Fig. 1**). All these fragments are well folded and show large α-helical content, as judged from their CD spectra (**Supplementary Fig. 2a**). Among these fragments, MUN-AB and MUN-CD did not stimulate the transition from the Munc18-1–syntaxin-1 complex to the SNARE complex, whereas MUN-ABC, MUN-BCD and MUN-BC exhibited a range of activities in stimulating the transition (**Fig. 3c**). These results identify subdomains B and C as the core region for MUN^{933} activity. Fragments MUN-ABC and MUN-BCD showed relatively higher activities than MUN-BC, but lower activity than MUN^{933}, thus suggesting that subdomains A and D have additional, albeit less critical, roles (compared to those of subdomains B and C) in stimulating Munc18-1–dependent SNARE-complex assembly.

Next, we aimed to identify key residues that mediate the activity of MUN^{933}. According to the MUN^{933} structure, we designed a series of mutations on the surface of subdomains B and C (**Supplementary Fig. 3a**). Using a native gel assay that we established (Online Methods and **Supplementary Fig. 3b**) and extensive screening, we found that residues Asn1128 and Phe1131 (referred to as NF) are crucial for the activity of MUN^{933} in promoting the transition from the Munc18-1–syntaxin-1 complex to the SNARE complex (**Supplementary Fig. 3c**). FRET experiments confirmed this finding by showing that double mutation of NF to alanine (NFAA) totally disrupted the activity of MUN^{933} (**Fig. 3d,e**). We observed no activity even when the concentration of NFAA was elevated to 100 μM (data not shown), thus showing the critical importance of the NF sequence. Notably, CD

Table 1 Data collection and refinement statistics

	Munc13-1 MUN^{933}
Data collection	
Space group	$P2_12_12$
Cell dimensions	
a, *b*, *c* (Å)	114.1, 270.9, 47.7
α, β, γ (°)	90.0, 90.0, 90.0
Resolution (Å)	50.0–2.9 (2.95–2.90)
R_{merge} (%)	6.9 (63.4)
$I/\sigma I$	27.3 (1.95)
Completeness (%)	99.3 (98.7)
Redundancy	5.4 (5.1)
Refinement	
Resolution (Å)	50.0–2.9 (2.97–2.90)
No. reflections	32,104 (1,712)
R_{work} / R_{free}	0.217 / 0.252
No. atoms	
Protein	4,347
B factors	
Protein	85.4
r.m.s. deviations	
Bond lengths (Å)	0.006
Bond angles (°)	1.384

Values in parentheses are for highest-resolution shell.

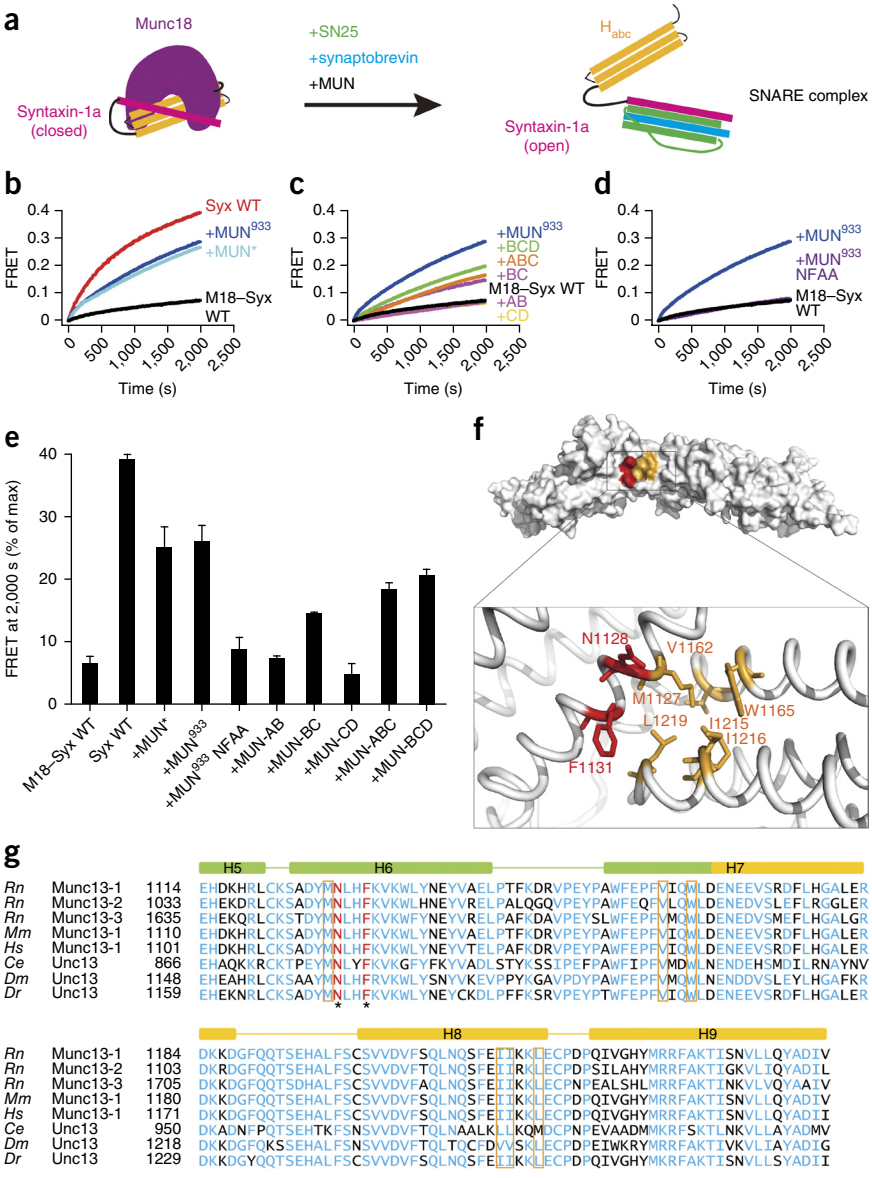

Figure 3 A conserved hydrophobic pocket that mediates the stimulatory activity of MUN^{933} in the transition from the Munc18-1–syntaxin-1 complex to the SNARE complex. (**a**) Illustration of FRET assay to detect SNARE-complex assembly. (**b–d**) FRET experiments showing the FRET between a BODIPY FL fluorescence donor on SNAP-25 (SN25) and a rhodamine fluorescence acceptor on syntaxin-1$_{2–253}$ within the Munc18–syntaxin-1$_{2–253}$ complex (M18–Syx). The stimulation caused by MUN^{933}, MUN*, the MUN^{933} fragments and the NFAA mutant are shown, as indicated. (**e**) Quantification of the stimulation activities obtained in **b–d** (means ± s.d.; $n = 3$ technical replicates). (**f**) Position of the hydrophobic pocket in MUN^{933} and enlarged view of its structure. The conserved residues forming the pocket are labeled and colored in yellow, and residues Asn1128 and Phe1131 are colored in red. (**g**) Sequence alignment of the hydrophobic pocket region shared in UNC-13-Munc13 species. Red and asterisk, residues Asn1128 and Phe1131; yellow box, conserved residues in the pocket; cyan, other conserved residues; *Rn*, *Rattus norvegicus*; *Mm*, *Mus musculus*; *Hs*, *Homo sapiens*; *Ce*, *C. elegans*; *Dm*, *Drosophila melanogaster*; *Dr*, *Danio rerio*.

spectroscopy and gel filtration showed that the NFAA mutant is well folded and exhibits similar CD spectra, denaturation curves and elution volume as MUN^{933} (**Supplementary Fig. 2b,c**). These results rule out the possibility that loss of activity is caused by protein misfolding.

In the structure of MUN^{933}, the NF residues reside next to each other on the surface of helix H6 in subdomain B. H6 packs against helices H7 and H8 in an antiparallel and parallel manner, respectively, with Met1127 on H6, Val1162 and Trp1165 on H7, and Ile1215, Ile1216 and Leu1219 on H8 forming a shallow hydrophobic pocket (**Fig. 3f**). Thus, this hydrophobic pocket built by these highly conserved residues is formed by residues from subdomains B and C at the junction between the two domains (**Fig. 3f**), results indicating that the loss of function of MUN-AB and MUN-CD arises because the integrity of the hydrophobic pocket is broken. Importantly, sequence alignments showed that the NF residues are highly conserved in UNC-13-Munc13 proteins (**Fig. 3g**). Together, these data show that the hydrophobic pocket, especially the conserved NF residues, are central for the activity of the MUN domain in opening syntaxin-1.

The NF sequence is crucial for proteoliposome fusion

The FRET experiments showed the importance of the NF sequence for the ability of the MUN domain to mediate the transition from the Munc18-1–syntaxin-1 complex to the SNARE complex in solution. We next sought to verify the key role of the NF sequence in SNARE-mediated membrane fusion.

Our newly established *in vitro* reconstitution assay[25] has recently reproduced the vital functions of Munc18-1 and Munc13-1 in neurotransmitter release. In this assay, instead of using syntaxin-1–SNAP-25 liposomes, we used liposomes reconstituted with Munc18-1–syntaxin-1 complex to start fusion reactions with synaptobrevin-containing liposomes and monitored lipid mixing and content mixing by fluorescence dequenching methods[25,34]. For these experiments, we used a Munc13-1 fragment that contains the diacylglycerol-binding C_1 domain, the phosphatidylinositol 4,5 bisphosphate–binding C_2B domain and the MUN domain (residues 529–1407, EF, 1453–1531; referred to as C_1-C_2B-MUN (**Fig. 1**)) because this fragment is much more efficient than the isolated MUN domain, owing to the membrane interactions of the C_1 and C_2B domains[25]. We observed virtually no lipid mixing or content mixing between Munc18-1–syntaxin-1 liposomes and synaptobrevin liposomes when adding SNAP-25 and syntaptotagmin-1 C_2AB in the presence of Ca^{2+} (**Fig. 4**). Further addition of 1 μM Munc13-1 C_1-C_2B-MUN dramatically facilitated the SNARE-mediated lipid mixing and content mixing (**Fig. 4**). However, C_1-C_2B-MUN containing the NFAA double mutation completely abolished such activity in stimulating both lipid mixing and content mixing (**Fig. 4b,e**). These data demonstrate that the NF sequence is critical for the activity of Munc13-1 in SNARE-mediated membrane fusion. We also note that C_2AB was critical for content mixing in the experiments with WT C_1-C_2B-MUN (**Fig. 4e,f**), as described previously[25].

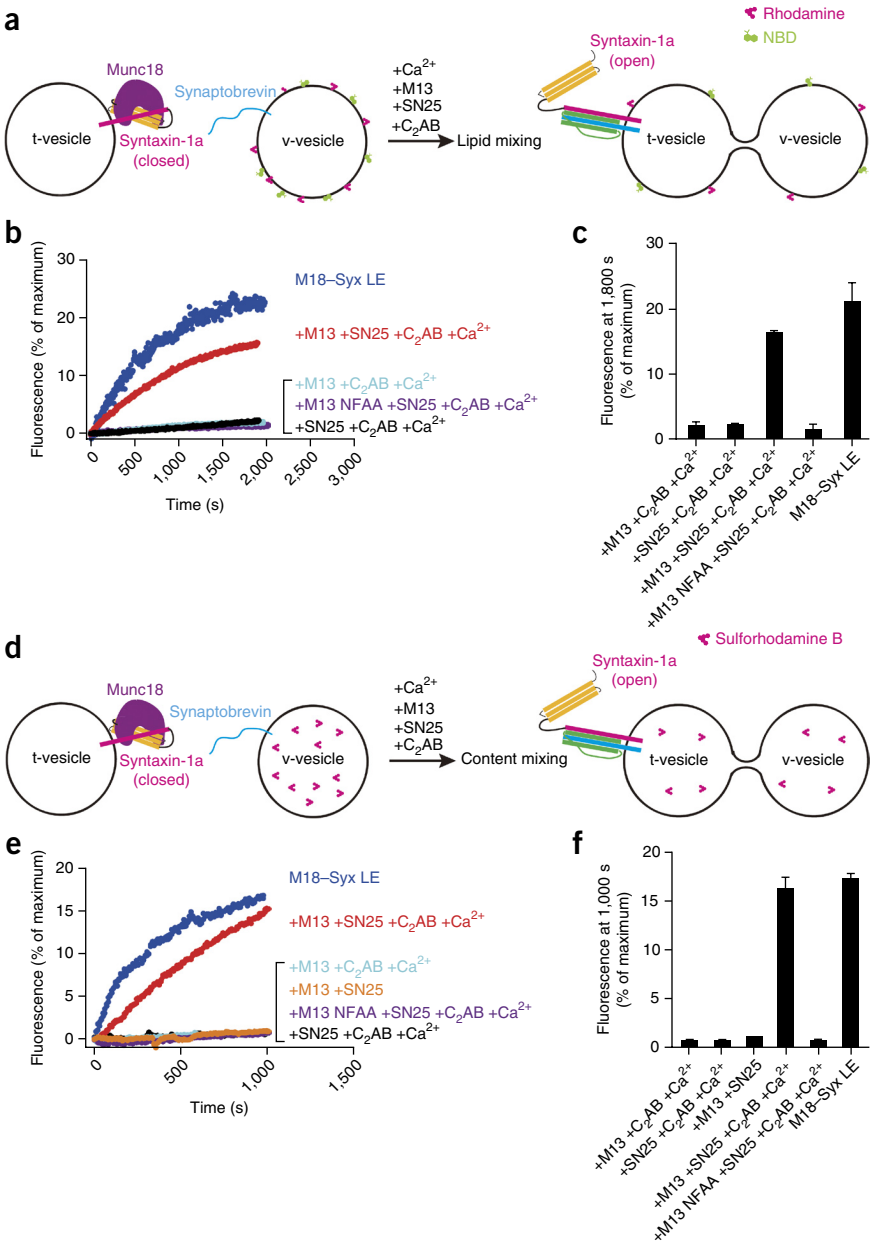

Figure 4 The Munc13-1 NFAA mutation abolishes SNARE-mediated liposome fusion. (**a**) Illustration of the lipid-mixing experiment (Online Methods). The donor liposomes (v-vesicles) contain synaptobrevin, whereas the acceptor liposomes (t-vesicles) contain the Munc18-1–syntaxin-$1_{1–288}$ complex or its LE mutant (M18–Syx LE). NBD, 7-nitrobenz-2-oxa-1,3-diazol label. (**b**) Lipid-mixing experiments confirming the critical role of the NF sequence. The experiments were performed in the presence of SNAP-25, synaptotagmin-1 cytoplasmic region (C_2AB), C_1-C_2B-MUN (M13) and/or the NFAA mutant, and 0.5 mM Ca^{2+} as indicated. (**c**) Quantification of the results obtained (means ± s.d.; $n = 3$ technical replicates). (**d**) Illustration of the content-mixing experiment (Online Methods), in which sulforhodamine fluorescence is dequenched as donor and acceptor liposomes merge. (**e**) Content-mixing experiments confirming the critical role of the NF sequence. (**f**) Quantification of the results obtained (means ± s.d.; $n = 3$ technical replicates). SN25, SNAP-25.

Previous studies have shown that the syntaxin-1 LE mutation, which helps to open syntaxin-1, partially rescues release in *unc-13*–null *C. elegans* and suppresses the block caused by Munc18-1 in SNARE-complex formation, thus suggesting that UNC-13-Munc13s are involved in opening syntaxin-1 (refs. 15,23). In our study, we tested whether the syntaxin-1 LE mutation could rescue membrane fusion in the absence of Munc13-1. Indeed, efficient lipid mixing and content mixing between Munc18-1–syntaxin-1 LE liposomes and synaptobrevin liposomes were still observable in the absence of Munc13-1 and the presence of SNAP-25, C_2AB and Ca^{2+} (**Fig. 4b**,**e**). These data suggest that syntaxin-1 LE mutation reverses the blocking effect caused by Munc18-1 and further support the notion that UNC-13-Munc13s are involved in opening syntaxin-1.

The NF sequence is pivotal for synaptic-vesicle priming

The *in vitro* experiments above provide strong evidence that the NF sequence of Munc13-1 has a key role in opening syntaxin-1. Sequence alignments showed that the residues NF are highly conserved in UNC-13-Munc13s from different species (**Fig. 3g**). To investigate the function of the NF sequence *in vivo*, we took *C. elegans* UNC-13 as a model protein and studied its function in synaptic transmission at NMJs. The *C. elegans unc-13* gene, which is essential for synaptic-vesicle exocytosis[35], encodes long and short isoforms (UNC-13L and UNC-13S). Both of these isoforms share a common region containing the C_1, C_2B, MUN and C_2C domains (**Fig. 1**). UNC-13L or Munc13s (e.g., Munc13-1 and Munc13-2) have an additional N-terminal C_2A domain and a CaM-binding domain that UNC-13S lacks[36] (**Fig. 1**). Expression of either UNC-13L or UNC-13S in *unc-13*–mutant worms rescued locomotion and neurotransmission defects, thus indicating that both isoforms are able to restore synaptic-vesicle exocytosis[37]. It has also been shown that Munc13 mutants that lack N-terminal C_2A- and CaM-binding domains can rescue the priming defects of synaptic vesicles in the absence of Munc13s[20,38]. Hence, to minimize the complexity of our system, we used UNC-13S to assess the role of the NF sequence in synaptic function.

The *s69* allele of *unc-13* corresponds to a 5-bp deletion in an exon shared by UNC-13S and UNC-13L[39], which shifts the reading frame, thereby inactivating both isoforms. Consistently with previous findings[37], expression of UNC-13S in *unc-13(s69)* rescued the locomotion rate (to 32.25% that of wild-type worms; **Supplementary Fig. 4**). In contrast, when we mutated the NF residues to alanines (hereafter referred to as UNC-13S NFAA), the mutant failed to rescue the locomotion defects (**Supplementary Fig. 4**).

To directly characterize the role of the NF sequence in synaptic transmission, we recorded excitatory postsynaptic currents (EPSCs) at NMJs from adult body-wall muscles (**Fig. 5**). We analyzed both endogenous EPSCs, which represent spontaneous fusion of single synaptic vesicles under resting conditions, and evoked EPSCs, which

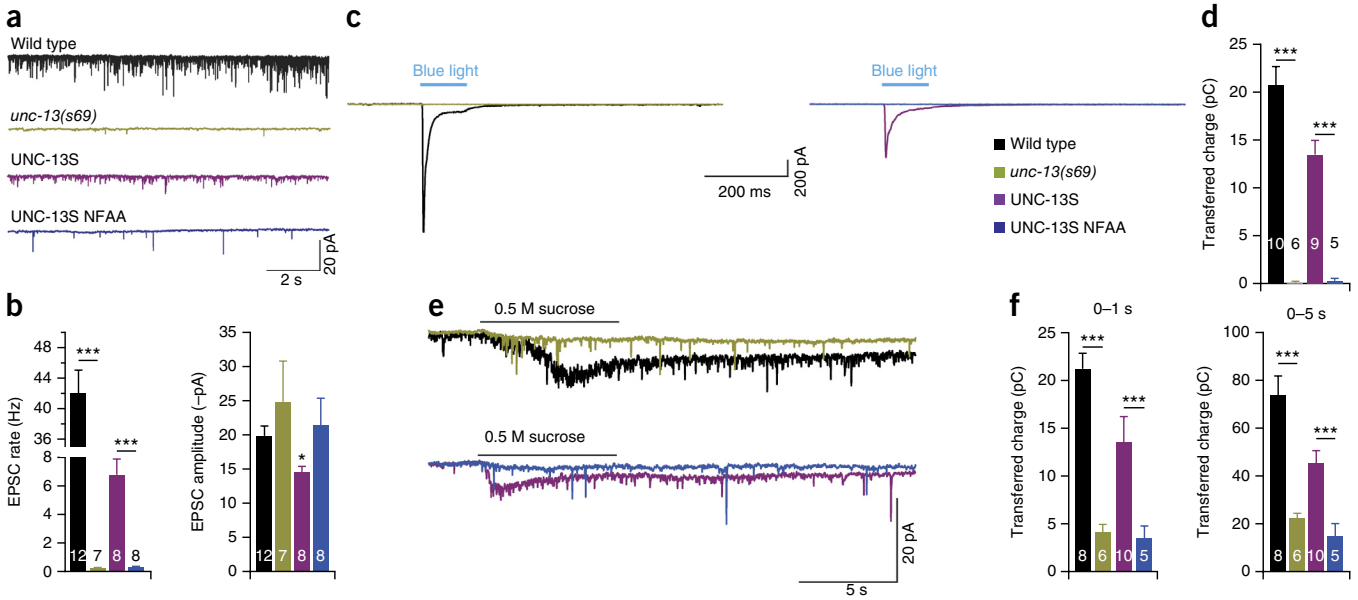

Figure 5 The UNC-13-Munc13 NFAA mutation abolishes synaptic-vesicle priming and exocytosis. (**a**,**b**) Recordings of endogenous EPSCs from adult body-wall muscles of the indicated genotypes. Representative traces (**a**) and summary data (**b**) are shown. (**c**,**d**) Recordings of photoevoked EPSCs from adult body-wall muscles of the indicated genotypes. Averaged traces (**c**) and cumulative charge transfer (**d**) are shown. (**e**,**f**) Average recording traces (**e**) and summary of transferred charges (**f**) of vesicle release induced by 0.5 M hypertonic sucrose solution in worms of the indicated genotypes. Values that differ significantly from controls are indicated (***$P < 0.001$; *$P < 0.05$ by two-tailed Student's *t* test). For each genotype, independent experiments were carried out in different animals, with the numbers of worms indicated in the graphs. Error bars, s.e.m.

represent Ca^{2+}-triggered exocytosis of hundreds of synaptic vesicles simultaneously. To minimize variation in recording evoked EPSCs, we used the optogenetic method by expressing ChR2 in presynaptic neurons and shining blue light (450–490 nm) on them to induce depolarization. *unc-13(s69)* worms exhibited neither spontaneous nor evoked EPSCs. Expressing UNC-13S in a *unc-13(s69)* background rescued the endogenous EPSC rate (to 16.22% that of wild type; **Fig. 5a**,**b**) and evoked EPSCs (to 64.73% that of wild type; **Fig. 5c**,**d**), consistently with previous results[37,40]. In contrast, the UNC-13S NFAA mutant completely failed to rescue both endogenous and Ca^{2+}-triggered evoked EPSCs (**Fig. 5a–d**), thus confirming the vital function of the NF sequence in synaptic-vesicle exocytosis.

The defect in presynaptic release of the UNC-13S NFAA mutant could be due to defective priming of synaptic vesicles or to a defect in the response of synaptic vesicles to Ca^{2+} influx. A classic assay to analyze priming involves the application of hypertonic sucrose solution to induce synaptic-vesicle exocytosis in a Ca^{2+}-independent manner; this is often used as a measure of the readily releasable pool of vesicles[41]. Here we used a prolonged sucrose-stimulation protocol[41] to release the majority of primed synaptic vesicles at *C. elegans* NMJs. Under this protocol, the sucrose-induced charge transfer observed in wild-type and *unc-13(s69)* worms were 21.29 ± 1.57 pC and 4.09 ± 0.82 pC, respectively, during 0–1 s, and 73.99 ± 7.78 pC and 22.31 ± 1.83 pC, respectively, during 0–5 s (**Fig. 5e**,**f**), comparably to previous results[40,42]. UNC-13S expression in *unc-13(s69)* worms rescued the sucrose-induced charge transfer to 13.54 ± 2.68 pC (to 63.60% that of wild type, **Fig. 5e**,**f**) during 0–1 s and 45.37 ± 5.15 pC during 0–5 s stimulation (to 61.32% that of wild type, **Fig. 5e**,**f**), whereas the UNC-13S NFAA mutant failed to rescue the sucrose-induced charge transfers (3.59 ± 1.03 pC during 0–1 s and 14.58 ± 5.37 pC during 0–5 s; **Fig. 5e**,**f**). These results reveal that the NF sequence is critical for both spontaneous and evoked release, and they indicate a key role for the NF sequence in the priming of synaptic vesicles.

DISCUSSION

UNC-13-Munc13s perform a crucial function in synaptic-vesicle priming, a step before Ca^{2+}-triggered release that is believed to involve opening of syntaxin-1 as well as SNARE-complex assembly[15,23]. Previous studies have suggested a pathway in which SNARE-complex assembly starts with the Munc18-1–syntaxin-1 complex and depends critically on regulation by the Munc13-1 MUN domain[15,25]. However, the physiological relevance of this model had been unclear because there was no evidence correlating the priming function of UNC-13-Munc13s *in vivo* with the activity of the MUN domain in opening syntaxin-1 *in vitro*. To bridge the gap between the understanding of the functional properties of the MUN domain and of its molecular features, we solved the crystal structure of the Munc13-1 MUN domain and identified key residues responsible for its activity in opening syntaxin-1. Moreover, the physiological data demonstrated the essential role of these residues in synaptic-vesicle priming. These results provide evidence that the critical function of the MUN domain in the transition of the Munc18-1–syntaxin-1 complex to the SNARE complex underlies the central function of UNC-13-Munc13s in synaptic-vesicle priming.

Crystallization of the UNC-13-Munc13 MUN domain has been a long-sought goal because this was the only essential element of the neurotransmitter-release machinery for which a three-dimensional structure had not been determined. The crystal structure of the rat Munc13-1 MUN domain described here reveals an elongated architecture formed by α-helical bundles, as expected from its predicted homology with tethering factors[26]. The structure enabled us to design a series of mutations in conserved surface residues to probe their importance in the ability of the MUN domain to open syntaxin-1. By using an *in vitro* SNARE complex–assembly assay, we identified a functionally critical, small hydrophobic pocket located at the junction of subdomains B and C. We showed that two highly conserved residues in this hydrophobic pocket, NF, have a key role in mediating

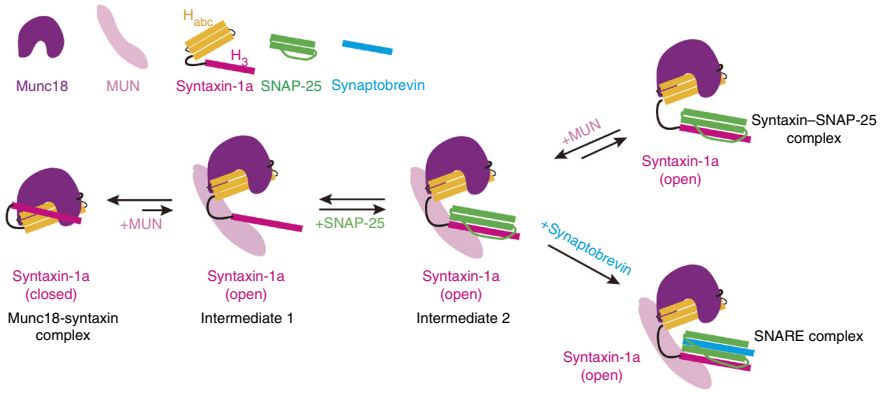

Figure 6 Working model for the mechanism underlying the activity of the MUN domain. The diagrams represent the Munc18-1–syntaxin-1 complex (left), the syntaxin-1–SNAP-25 complex bound to Munc18-1 (upper right) and the SNARE complex bound to Munc18-1 and the MUN domain (lower right) as well as intermediate states that are proposed to mediate the transitions between the different complexes. A key aspect of the model is that multiple weak interactions of the MUN domain with Munc18-1, syntaxin-1 and perhaps the other SNAREs lower the energy barriers involved in these transitions. Starting from the Munc18-1–syntaxin-1 complex, binding of the MUN domain to Munc18-1 and syntaxin-1 is proposed to transiently open syntaxin-1, thus leading to intermediate 1. Binding of SNAP-25 leads to intermediate 2, which can serve as substrate for SNARE-complex assembly (which is probably irreversible) upon synaptobrevin binding. Intermediate 2 could also be in the path leading from the syntaxin-1–SNAP-25 complex to the Munc18-1–syntaxin-1 complex in the absence of synaptobrevin. The relative size of the arrows illustrates the observation that Munc18-1 displaces SNAP-25 from syntaxin-1. The membranes are not shown but are also expected to influence the equilibria because of interactions with the MUN domain and perhaps with other components.

the transition from the Munc18-1–syntaxin-1 complex to the SNARE complex. The NF side chains face the surface of the hydrophobic pocket (**Fig. 3f**), thus providing a plausible binding contact for its potential 'substrate' (for example, syntaxin-1 or other SNAREs). Mutation of these residues to alanines (NFAA mutation) does not alter the folding of the MUN domain (**Supplementary Fig. 2**). Thus, the functional effects of the NFAA mutation must arise from disruption of specific interactions involving these side chains. We characterized these effects at three different levels: (i) SNARE-complex assembly in solution; (ii) SNARE-dependent liposome fusion in a reconstituted proteoliposome system; and (iii) synaptic transmission at NMJs in *C. elegans*. The drastic effects of the NFAA mutation at these three levels (**Figs. 3d**, **4** and **5**) demonstrate the vital nature of the NF sequence for MUN-domain function and leave little doubt that the impairment caused by this mutation on stimulation of SNARE-complex assembly and proteoliposome fusion underlies the abrogation of synaptic-vesicle priming caused by the mutation.

The observation that subdomains A and/or D enhance the activity of subdomains B and C in the SNARE complex–assembly assay (**Fig. 3c**,**e**) suggests that multiple sites of the MUN domain cooperate in catalyzing syntaxin-1 opening. The multiple interactions underlying the activity of the MUN domain probably involve Munc18-1 in addition to syntaxin-1, because the MUN domain accelerates SNARE-complex assembly starting from the Munc18-1–syntaxin-1 complex but not from isolated syntaxin-1 (ref. 15). Moreover, in cofloatation assays, we observed that the MUN domain binds to liposomes containing reconstituted Munc18-1–syntaxin-1 complex but not to liposomes containing isolated syntaxin-1 or syntaxin-1–SNAP-25 complex, and the MUN NFAA mutation disrupts binding to the Munc18-1–syntaxin-1 liposomes (**Supplementary Fig. 5**). These results suggest that interaction between the MUN-domain NF pocket and the Munc18-1–syntaxin-1 complex is key for opening syntaxin-1 and that membrane anchoring enhances the affinity of the MUN domain for the Munc18-1–syntaxin-1 complex. Such enhancement probably arises from weak interactions of basic regions of the MUN domain (**Supplementary Fig. 1a**) with the phospholipids. These multiple interactions are likely to underlie the finding that the MUN domain catalyzes not only the transition from the Munc18-1–syntaxin-1 complex to the SNARE complex but also the transition from the syntaxin-1–SNAP-25 complex to the Munc18-1–syntaxin-1 complex, as reported in our previous work[25]. These observations lead us to propose a working model of how UNC-13-Munc13s function (**Fig. 6**). Briefly, SNARE-complex formation is irreversible once synaptobrevin is available, whereas in the absence of synaptobrevin the equilibrium shifts toward the Munc18-1–syntaxin-1 complex because it is more stable than the syntaxin-1–SNAP-25 complex. The MUN domain lowers the energy barrier of the transitions between these complexes (**Fig. 6**, intermediate states).

Growing evidence has suggested that, in addition to mediating the opening of syntaxin-1 and the assembly of the SNARE complex, the UNC-13-Munc13 MUN domain functions in tethering vesicles to presynaptic active zones[43–45]. This tethering function should be favored by the elongated α-helix-bundle structure of the Munc13-1 MUN domain, which spans more than 150 Å and is similar to those of factors with known roles in tethering, such as Sec6p, Tip20 and Exo70. We suggest that the function of UNC-13-Munc13s in tethering depends on this elongated α-helical-bundle structure and probably on their association with other factors (for example, RIMs) to form a tethering complex[1]. Nevertheless, structure-based sequence alignments showed that key residues responsible for forming the NF pocket of UNC-13-Munc13s are not shared by other tethering proteins (**Supplementary Fig. 6**). Hence, these residues probably endow the UNC-13-Munc13 MUN domain with specificity in synaptic-vesicle priming.

Further research will be required not only to identify the target of the MUN NF pocket but also to elucidate the function and molecular mechanism of the MUN domain in tethering. The structure of the Munc13-1 MUN-domain structure described here provides a framework to design and interpret these studies.

METHODS

Methods and any associated references are available in the online version of the paper.

Accession codes. Coordinates and structure factors for MUN^{933} have been deposited in the Protein Data Bank under accession code 4Y21.

Note: Any Supplementary Information and Source Data files are available in the online version of the paper.

ACKNOWLEDGMENTS

We thank the BL19ID station at the Advanced Photon Source, Argonne National Laboratory, for helping with data collection. We thank J. Kaplan (Massachusetts

General Hospital) for providing the *unc-13(s69)* strain and the Caenorhabditis Genetic Center for providing other strains used in this work. We thank Y. Li and X. Wang of the Huazhong University of Science and Technology (HUST) for initial efforts in constructing MUN-domain mutations and M. Zhang (Hong Kong University of Science and Technology) for insightful comments on the manuscript. This work was supported by grant 31370819 from the National Science Foundation of China and grant 2014CB910203 from the National Key Basic Research Program of China (both to C.M.), grants (31130065 and 91313301) from the National Science Foundation of China (both to T.X.) and grant NS37200 from the US National Institutes of Health (to J.R.).

AUTHOR CONTRIBUTIONS

C.M., M.Z., L.W. and R.Z. performed the structural-biology experiments; X.Y. and S.W. generated all mutants used in this study and performed *in vitro* experiments of SNARE-complex assembly and liposome fusion; Y.S., W.Z. and L.K. performed *in vivo* electrophysiology experiments; T.X. and C.M. conceived the experiments; and J.R., T.X. and C.M. wrote the paper.

COMPETING FINANCIAL INTERESTS

The authors declare no competing financial interests.

1. Rizo, J. & Sudhof, T.C. The membrane fusion enigma: SNAREs, Sec1/Munc18 proteins, and their accomplices—guilty as charged? *Annu. Rev. Cell Dev. Biol.* **28**, 279–308 (2012).
2. Toonen, R.F. & Verhage, M. Munc18–1 in secretion: lonely Munc joins SNARE team and takes control. *Trends Neurosci.* **30**, 564–572 (2007).
3. Jahn, R. & Scheller, R.H. SNAREs: engines for membrane fusion. *Nat. Rev. Mol. Cell Biol.* **7**, 631–643 (2006).
4. Brunger, A.T., Weninger, K., Bowen, M. & Chu, S. Single-molecule studies of the neuronal SNARE fusion machinery. *Annu. Rev. Biochem.* **78**, 903–928 (2009).
5. Söllner, T., Bennett, M.K., Whiteheart, S.W., Scheller, R.H. & Rothman, J.E. A protein assembly-disassembly pathway *in vitro* that may correspond to sequential steps of synaptic vesicle docking, activation, and fusion. *Cell* **75**, 409–418 (1993).
6. Hanson, P.I., Roth, R., Morisaki, H., Jahn, R. & Heuser, J.E. Structure and conformational changes in NSF and its membrane receptor complexes visualized by quick-freeze/deep-etch electron microscopy. *Cell* **90**, 523–535 (1997).
7. Poirier, M.A. *et al.* The synaptic SNARE complex is a parallel four-stranded helical bundle. *Nat. Struct. Biol.* **5**, 765–769 (1998).
8. Sutton, R.B., Fasshauer, D., Jahn, R. & Brunger, A.T. Crystal structure of a SNARE complex involved in synaptic exocytosis at 2.4 Å resolution. *Nature* **395**, 347–353 (1998).
9. Dulubova, I. *et al.* A conformational switch in syntaxin during exocytosis: role of munc18. *EMBO J.* **18**, 4372–4382 (1999).
10. Misura, K.M., Scheller, R.H. & Weis, W.I. Three-dimensional structure of the neuronal-Sec1–syntaxin 1a complex. *Nature* **404**, 355–362 (2000).
11. Gerber, S.H. *et al.* Conformational switch of syntaxin-1 controls synaptic vesicle fusion. *Science* **321**, 1507–1510 (2008).
12. Rizo, J., Chen, X. & Arac, D. Unraveling the mechanisms of synaptotagmin and SNARE function in neurotransmitter release. *Trends Cell Biol.* **16**, 339–350 (2006).
13. Dulubova, I. *et al.* Munc18-1 binds directly to the neuronal SNARE complex. *Proc. Natl. Acad. Sci. USA* **104**, 2697–2702 (2007).
14. Shen, J., Tareste, D.C., Paumet, F., Rothman, J.E. & Melia, T.J. Selective activation of cognate SNAREpins by Sec1/Munc18 proteins. *Cell* **128**, 183–195 (2007).
15. Ma, C., Li, W., Xu, Y. & Rizo, J. Munc13 mediates the transition from the closed syntaxin–Munc18 complex to the SNARE complex. *Nat. Struct. Mol. Biol.* **18**, 542–549 (2011).
16. Augustin, I., Rosenmund, C., Sudhof, T.C. & Brose, N. Munc13-1 is essential for fusion competence of glutamatergic synaptic vesicles. *Nature* **400**, 457–461 (1999).
17. Varoqueaux, F. *et al.* Total arrest of spontaneous and evoked synaptic transmission but normal synaptogenesis in the absence of Munc13-mediated vesicle priming. *Proc. Natl. Acad. Sci. USA* **99**, 9037–9042 (2002).
18. Richmond, J.E., Davis, W.S. & Jorgensen, E.M. UNC-13 is required for synaptic vesicle fusion in *C. elegans*. *Nat. Neurosci.* **2**, 959–964 (1999).
19. Aravamudan, B., Fergestad, T., Davis, W.S., Rodesch, C.K. & Broadie, K. *Drosophila* UNC-13 is essential for synaptic transmission. *Nat. Neurosci.* **2**, 965–971 (1999).
20. Basu, J. *et al.* A minimal domain responsible for Munc13 activity. *Nat. Struct. Mol. Biol.* **12**, 1017–1018 (2005).
21. Madison, J.M., Nurrish, S. & Kaplan, J.M. UNC-13 interaction with syntaxin is required for synaptic transmission. *Curr. Biol.* **15**, 2236–2242 (2005).
22. Stevens, D.R. *et al.* Identification of the minimal protein domain required for priming activity of Munc13-1. *Curr. Biol.* **15**, 2243–2248 (2005).
23. Richmond, J.E., Weimer, R.M. & Jorgensen, E.M. An open form of syntaxin bypasses the requirement for UNC-13 in vesicle priming. *Nature* **412**, 338–341 (2001).
24. Koushika, S.P. *et al.* A post-docking role for active zone protein Rim. *Nat. Neurosci.* **4**, 997–1005 (2001).
25. Ma, C., Su, L., Seven, A.B., Xu, Y. & Rizo, J. Reconstitution of the vital functions of Munc18 and Munc13 in neurotransmitter release. *Science* **339**, 421–425 (2013).
26. Pei, J., Ma, C., Rizo, J. & Grishin, N.V. Remote homology between Munc13 MUN domain and vesicle tethering complexes. *J. Mol. Biol.* **391**, 509–517 (2009).
27. Yu, I.M. & Hughson, F.M. Tethering factors as organizers of intracellular vesicular traffic. *Annu. Rev. Cell Dev. Biol.* **26**, 137–156 (2010).
28. Sivaram, M.V., Furgason, M.L., Brewer, D.N. & Munson, M. The structure of the exocyst subunit Sec6p defines a conserved architecture with diverse roles. *Nat. Struct. Mol. Biol.* **13**, 555–556 (2006).
29. Li, W. *et al.* The crystal structure of a Munc13 C-terminal module exhibits a remarkable similarity to vesicle tethering factors. *Structure* **19**, 1443–1455 (2011).
30. Rizo, J. & Rosenmund, C. Synaptic vesicle fusion. *Nat. Struct. Mol. Biol.* **15**, 665–674 (2008).
31. Tripathi, A., Ren, Y., Jeffrey, P.D. & Hughson, F.M. Structural characterization of Tip20p and Dsl1p, subunits of the Dsl1p vesicle tethering complex. *Nat. Struct. Mol. Biol.* **16**, 114–123 (2009).
32. Dong, G., Hutagalung, A.H., Fu, C., Novick, P. & Reinisch, K.M. The structures of exocyst subunit Exo70p and the Exo84p C-terminal domains reveal a common motif. *Nat. Struct. Mol. Biol.* **12**, 1094–1100 (2005).
33. Moore, B.A., Robinson, H.H. & Xu, Z. The crystal structure of mouse Exo70 reveals unique features of the mammalian exocyst. *J. Mol. Biol.* **371**, 410–421 (2007).
34. Weber, T. *et al.* SNAREpins: minimal machinery for membrane fusion. *Cell* **92**, 759–772 (1998).
35. Richmond, J.E., Davis, W.S. & Jorgensen, E.M. UNC-13 is required for synaptic vesicle fusion in *C. elegans*. *Nat. Neurosci.* **2**, 959–964 (1999).
36. Brose, N., Rosenmund, C. & Rettig, J. Regulation of transmitter release by Unc-13 and its homologues. *Curr. Opin. Neurobiol.* **10**, 303–311 (2000).
37. Hu, Z., Tong, X.J. & Kaplan, J.M. UNC-13L, UNC-13S, and Tomosyn form a protein code for fast and slow neurotransmitter release in *Caenorhabditis elegans*. *eLife* **2**, e00967 (2013).
38. Deng, L., Kaeser, P.S., Xu, W. & Südhof, T.C. RIM proteins activate vesicle priming by reversing autoinhibitory homodimerization of Munc13. *Neuron* **69**, 317–331 (2011).
39. Rose, A.M. & Baillie, D.L. Genetic organization of the region around UNC-15 (I), a gene affecting paramyosin in *Caenorhabditis elegans*. *Genetics* **96**, 639–648 (1980).
40. Zhou, K., Stawicki, T.M., Goncharov, A. & Jin, Y. Position of UNC-13 in the active zone regulates synaptic vesicle release probability and release kinetics. *eLife* **2**, e01180 (2013).
41. Rosenmund, C. & Stevens, C.F. Definition of the readily releasable pool of vesicles at hippocampal synapses. *Neuron* **16**, 1197–1207 (1996).
42. Gracheva, E.O. *et al.* Tomosyn inhibits synaptic vesicle priming in *Caenorhabditis elegans*. *PLoS Biol.* **4**, e261 (2006).
43. Hammarlund, M., Palfreyman, M.T., Watanabe, S., Olsen, S. & Jorgensen, E.M. Open syntaxin docks synaptic vesicles. *PLoS Biol.* **5**, e198 (2007).
44. Siksou, L. *et al.* A common molecular basis for membrane docking and functional priming of synaptic vesicles. *Eur. J. Neurosci.* **30**, 49–56 (2009).
45. Weimer, R.M. *et al.* UNC-13 and UNC-10/rim localize synaptic vesicles to specific membrane domains. *J. Neurosci.* **26**, 8040–8047 (2006).

ONLINE METHODS

Recombinant-protein purification. Full-length rat synaptobrevin-2 and its cytoplasmic domain (residues 29–93), full-length rat syntaxin-1a and its cytoplasmic domain (residues 2–253), full-length human SNAP-25A (with its four cysteines mutated to serines) and its SNARE motifs (SN1, residues 11–82; SN3, residues 141–203), full-length rat Munc18-1, squid Munc18-1, rat Munc13-1 MUN* domain (residues 859–1407, EF, 1453–1531), C1-C2B-MUN domain (residues 529–1407, EF, 1453–1531), coexpressed Munc18-1–syntaxin-1, and rat synaptotagmin-1 cytoplasmic domain C_2AB (residues 140–421) were expressed and purified as described previously[8,9,13,15,20,25]. Recombinant rat Munc13-1 MUN^{933} (residues 933–1407, EF, 1453–1531) was expressed in BL21 *Escherichia coli* cells as a GST-fusion protein, with a pGEX-KG vector (GE Healthcare). GST-MUN^{933} was first purified on a glutathione–Sepharose 4B (GE Healthcare) affinity column; this was followed by removal of the GST tag with thrombin overnight at 4 °C. Further purification was carried out by successive chromatography steps on a Resource Q anion-exchange column and Superdex-200 16/600 column (GE Healthcare). Finally, MUN^{933} in a buffer containing 20 mM Tris (hydroxymethyl) aminomethane (Tris), pH 8.5, 150 mM NaCl, 10% glycerol (v/v) (buffer A) and 5 mM DL-dithiothreitol (DTT) was concentrated to 9–10 mg/ml for crystallization. Mutants and fragments of the MUN domain, including MUN^{933} NFAA, MUN-ABC (residues 859–1407), MUN-AB (residues 933–1167), MUN-BCD (residues 1011–1407, EF, 1453–1531), MUN-BC (residues 1011–1407), and MUN-CD (residues 1148–1407, EF, 1453–1531) were expressed, purified and concentrated as described for MUN^{933}. C1-C2B-MUN NFAA was expressed and purified as described previously[25] in insect cells (sf9). Protein concentrations were determined with a UV-visible spectrometer (SHIMADZU UV-2450). All the regents were analytical pure grade.

Protein crystallization and structure determination. Crystals were grown by the hanging-drop vapor-diffusion method at 4 °C. Purified tag-free MUN^{933} at 9–10 mg/ml in buffer A and 5 mM DTT was mixed with an equal volume of precipitant solution containing 18–25% PEG 3350 (v/v), 0.1 M MES, pH 5.8–6.3, and 0.2 M $Mg(NO_3)_2$. Full-size crystals were cryoprotected by soaking in harvesting liquor supplemented with 30% glycerol (v/v) before flash cooling in liquid nitrogen. X-ray diffraction data were collected at beamline 19ID (Advanced Photon Source (APS), Argonne National Laboratory). Data were processed with HKL2000 (ref. 46). The primary model of the MUN^{933} was determined by molecular replacement with the MUN-CD (PDB 3SWH[29]) as a starting model. Molecular replacement was performed with Phaser[47]. Then a model completion was performed with the pipeline IPCAS (OASIS4.2, available at http://cryst.iphy.ac.cn/), which gave an almost-complete model of the protein. The model was manually improved in COOT[48] and iteratively refined by Refmac[49]. In the final model, more than 97% of residues fell in the favored region in the Ramachandran plot, and the final R_{work}/R_{free} values are 0.212/0.252. Data collection and refinement statistics are listed in **Table 1**.

Circular dichroism spectroscopy. MUN^{933}, its fragments and the mutant NFAA were diluted to a concentration of 0.1 mg/ml in buffer A and 0.1 mM Tris (2-carboxyethyl) phosphine (TCEP, Sigma-Aldrich). CD spectra were recorded with a JASCO J-810 Spectropolarimeter at 25 °C from 200 nm to 250 nm with a cuvette with 1-mm path length. Thermal denaturation was recorded with a MOS-500 Spectropolarimeter (Bio-Logic) at absorption of 222 nm from 25 °C to 95 °C at 1-mm bandwidth.

Time-based fluorescence resonance energy transfer (FRET) assay. Rat syntaxin-1 (residues 2–253, C145S, S249C) and human SNAP-25A SN3 (residues 141–203, S187C) were labeled with tetramethylrhodamine-5-maleimide, single isomer (TMR, Molecular Probes) and BODIPY-FL maleimide (Molecular Probes), respectively. Protein labeling was performed by addition of 20-fold molar excess of dyes in a buffer containing 20 mM sodium phosphate, pH 7.4, 100 mM NaCl (buffer B) and 1 mM TCEP overnight at 4 °C. Labeled proteins were purified by PD-10 desalting columns (GE Healthcare) in a buffer containing 25 mM 4-(2-hydroxyethyl)-1-piperazineethanesulfonic acid (HEPES), pH 7.4, 150 mM KCl, 10% glycerol (v/v) (buffer C) and 2 mM DTT (for BODIPY-FL–labeled SNAP-25A SN3) or anion-exchange chromatography (for TMR-labeled syntaxin-1); this was followed by gel filtration in buffer C to remove free dyes. In the reaction, BODIPY-FL–labeled SNAP-25A SN3 was added at a final concentration of 2 μM, TMR labeled syntaxin-1 (preincubated or not with squid Munc18) was at 10 μM, and MUN*, MUN^{933} and its fragments and mutants were at 30 μM. Each experiment was repeated at least three times, and FRET efficiency was calculated according to $E = (F_0 - F_{obs})/F_0$, where F_0 is the initial fluorescence intensity, and F_{obs} is the fluorescence intensity measured as a function of time. Because of the limited solubility of rat Munc18-1, addition of isolated Munc18-1 at concentrations above 20 μM was done with squid Munc18-1, which is more soluble and has a 66.4% sequence identity with rat Munc18-1 as well as very similar biochemical properties[15].

Native gel assay. The reactions were initiated by addition of purified Munc18-1 and syntaxin-1 (residues 2–253) with a protein/protein ratio of 1.2:1; they were then incubated with synaptobrevin-2 (residues 29–93), SNAP-25A and excess of MUN^{933} or its mutants at room temperature for 2 h. Nondenaturing gels were prepared with 15% (w/v) polyacrylamide (acrylamide/bisacrylamide, 29:1) for the resolving gel and 4% (w/v) for the stacking gel. The electrophoresis buffer was composed of 25 mM Tris, 250 mM glycine, pH 8.3. Approximately 5 μl of each reaction sample was loaded per well and subjected to electrophoresis overnight at 4 °C at 80 V. The complex of Munc18-1 with syntaxin-1 (Munc18–Syx) displays sharp and clear bands in native gels, whereas other proteins or complexes show smeared bands. Each reaction was repeated at least three times, and the quantification of the Munc18–Syx bands was obtained by Image J (NIH).

Lipid-mixing and content-mixing assays. Proteoliposomes were prepared with established procedures[25]. Donor (synaptobrevin-2, v-) liposomes contained 60% POPC, 17% POPE and 20% DOPS. Acceptor (Munc18-1–syntaxin-1, t-) liposomes contained 58% POPC, 15% POPE, 20% DOPS, 2% PIP2 and 5% DAG. (All phospholipids were purchased from Avanti Polar Lipids.) Lipid mixtures were dried in glass tubes with nitrogen gas and subjected to vacuum for at least 5 h. Lipid films were resuspended in buffer C with 1 mM DTT and 1% 3-[(3-cholamidopropyl) dimethylammonio] propanesulfonate (CHAPS) (w/v, Amersco) and vortexed for 15 min. Purified proteins in buffer C containing 1% CHAPS (w/v) were added slowly to micelles at a final concentration of 5 mM total lipids. The protein/lipid ratio for v-liposomes was about 1:500, whereas the protein/lipid ratio for t-liposomes was about 1:1,000. The liposome-protein mixtures were incubated at room temperature for 30 min; this was followed by dialysis against buffer C and 1 mM DTT, 1 g/L Bio-Beads SM2 (Bio-Rad) three times at 4 °C in order to remove the detergent extensively. For lipid-mixing assays, v-liposomes (0.25 mM total lipids) containing 1.5% NBD-PE and 1.5% rhodamine-PE were mixed with t-liposomes (0.5 mM lipids) in the presence of ~0.5–1.0 μM C1-C2B-MUN (M13) or C1-C2B-MUN NFAA (M13 NFAA), 5 μM SNAP-25A, 2 μM C_2AB fragment (residues 140–421) and/or 0.5 mM Ca^{2+} (as indicated in the figures) in a total volume of 60 μl. NBD fluorescence emission at 538 nm (excitation 460 nm) was monitored with a PTI QM-40 spectrofluorometer. For content-mixing assays, v-liposomes were dissolved in buffer C containing 1% w/v β-OG and 40 mM sulforhodamine B (Sigma), purified full-length synaptobrevin-2 in buffer containing 1% w/v β-OG was added to the lipid mixtures to make the final concentration of lipids 2 mM and the P/L ratio 1:500. The proteoliposome was first dialyzed in small volume in buffer C containing 40 mM sulforhodamine B; this was followed by dialysis in buffer C containing 1 mM DTT and 1 g/L Bio-Beads three times at 4 °C (two times for 2 h and one time overnight). To remove remnant detergents, t-liposomes were prepared with the same method described for the lipid-mixing assays. Content mixing was monitored as described for the lipid-mixing assays by measurement of dequenching of sulforhodamine B (excitation at 565 nm, emission at 587 nm). The data were analyzed and quantified as described above for the lipid-mixing assays. All experiments were performed at 30 °C at least three times. At the end of each reaction, 1% CHAPS (w/v) was added to solubilize the liposomes. For more-consistent results, the time traces were converted to F_{obs}/F_0, where F_{obs} is the observed fluorescence intensity, and F_0 is the initial intensity. The F_{obs}/F_0 value observed upon detergent addition for an entire set of experiments was averaged. This average was finally used to normalize all the traces to display the data as a percentage of maximum fluorescence. The relative efficiencies resulting from different additions were reproducible in separate sets of experiments.

Liposome coflotation assay. Munc18-1–syntaxin-1, syntaxin-1 and syntaxin-1–SNAP-25 liposomes containing PC/PE/PS (60%:20%:20%) with a protein/

lipid (P/L) ratio of 1:800 were prepared with the same method described for the liposome-fusion assays. The liposomes (3.5 mM total lipids) were incubated with 10 µM MUN^{933} or MUN^{933} NFAA for 3 h at 16 °C. The proteoliposomes and bound proteins were isolated by flotation on a Histodenz density gradient (40%:35%:30%), as previously described[25]. Samples on the top (40 µl) were taken and analyzed by SDS-PAGE and Coomassie blue staining.

Strains. Strain maintenance and genetic manipulation were performed as previously described[50]. Worms were cultivated at 20 °C on agar nematode growth medium seeded with OP50 bacteria. The following strains were used in this study:

Wild type, N2 bristol
unc-13(s69)
Ex [P*snb-1*::UNC-13S]; *unc-13(s69)*
Ex [P*snb-1*::UNC-13S NFAA]; *unc-13(s69)*
ST422, zxIs6 [P*unc*-17::chop-2(H134R)::YFP; LIN-15]
zxIs6 [P*unc*-17::chop-2(H134R)::YFP; LIN-15]; *unc-13(s69)*
Ex [P*snb-1*::UNC-13S]; zxIs6 [P*unc*-17::chop-2(H134R)::YFP; LIN-15]; *unc-13(s69)*
Ex [P*snb-1*::UNC-13S NFAA]; zxIs6 [P*unc*-17::chop-2(H134R)::YFP; LIN-15]; *unc-13(s69)*

Transgenic strains were isolated by microinjection of various plasmids with P*lin-44*::GFP as coinjection markers. Plasmid encoding UNC-13S was a gift from J. Kaplan's laboratory, as previously described[37]. For UNC-13S NFAA, amino acid coordinates corresponding to residues Asn1128 and Phe1131 of Munc13-1 were mutated to alanines in UNC-13S cDNA. For electrophysiological recordings and locomotion behavior assays, transgenes were expressed by the *snb-1* promoter.

Locomotion and behavior assays. Worm tracking and analysis were performed as previously described[51]. Briefly, worms were reared at 20 °C and moved to room temperature 30 min before imaging. Young-adult animals were randomly picked to agar plates with no bacterial lawn (30 worms per plate). For locomotion assays, worms were randomly picked, and locomotion was analyzed 10 min after the worms were removed from food. A WAT-902H2 camera (Automatic System, Inc.) was used to capture high-contrast dark-field images of the assay plates. The behavior movies were taped at 1× magnification with a ZEISS V8 microscope at 25 Hz. These data were analyzed automatically by a home-written object-tracking plugin in ImageJ (http://imagej.nih.gov/ij/). Locomotion speed and the 30-s crawling trail were determined by ImageJ plugin.

Electrophysiology. Electrophysiology assays were performed at the neuromuscular junctions of dissected *C. elegans* under an Olympus microscope (BX51WI) with an EPC-10 amplifier and Patchmaster software (HEKA), as previously described[52,53]. Recording pipettes were pulled from borosilicate glass capillaries (Sutter Instruments) to a resistance of 3–4 MΩ on a P-97 micropipette puller (Sutter Instruments). Day 2 worms were glued on the surface of Sylgard-coated coverslips with cyanoacrylate-based glue. A dorsolateral incision was made with sharp glass pipettes, and a cuticle flap was then folded and glued down to the coverslip to expose the body-wall muscles. The preparation was treated by collagenase type IV (Sigma-Aldrich) for 30 s at a concentration of 0.4 mg/ml at 20 °C. The bath solution contained 127 mM NaCl, 5 mM KCl, 26 mM $NaHCO_3$, 1.25 mM NaH_2PO_4, 2 mM $CaCl_2$, 4 mM $MgCl_2$ and 10 mM glucose (325–335 mOsm, pH 7.3). The pipette solution contained 120 mM CH_3O_3SCs, 4 mM CsCl, 15 mM CsF, 4 mM $MgCl_2$, 5 mM EGTA, 0.25 mM $CaCl_2$, 10 mM HEPES and 4 mM Na_2-ATP (315–325 mOsm, pH 7.2). Membrane potential was clamped at −60 mV. The ZXIS6 strain, in which light-gated cation channel channelrhodopsin-2 (ChR2)-YFP was expressed in cholinergic neurons, was used for recording evoked EPSCs[54]. All-*trans* retinal was added to the NGM plates at a final concentration of 2.5 µM to mediate light stimulation of ChR2. L4 worms were transferred to NGM plates containing all-*trans* retinal, and next-generation hermaphrodite adults were used. For depletion of the readily releasable pool, the 0.5 M sucrose in bath solution was applied to the ventral nerve cord near the recorded muscles by an IM-300 microinjector (Narishige) with 8 psi for 5 s (ref. 40). Signals were filtered at 2 kHz, sampled at 20 kHz, and analyzed with IGOR Pro (Wavemetrics).

Statistical analysis. Statistical significance was determined by two-tailed Student's *t* tests. Experimental data meet the assumptions of normal distribution. For behavior and electrophysiology assays of worms, the sample size was chosen on the basis of previous studies[37,40] with no inclusion/exclusion criteria. The variances were similar between the groups being statistically compared. The investigators were not blinded to the group allocation during the experiments and data analysis.

46. Otwinowski, Z. & Minor, W. Processing of X-ray diffraction data collected in oscillation mode. *Methods Enzymol.* **276**, 307–326 (1997).
47. McCoy, A.J. *et al.* Phaser crystallographic software. *J. Appl. Crystallogr.* **40**, 658–674 (2007).
48. Emsley, P., Lohkamp, B., Scott, W.G. & Cowtan, K. Features and development of Coot. *Acta Crystallogr. D Biol. Crystallogr.* **66**, 486–501 (2010).
49. Vagin, A.A. *et al.* REFMAC5 dictionary: organisation of prior chemical knowledge and guidelines for its use. *Acta Crystallogr. D Biol. Crystallogr.* **60**, 2184–2195 (2004).
50. Brenner, S. The genetics of *Caenorhabditis elegans*. *Genetics* **77**, 71–94 (1974).
51. Yue, Y. *et al.* The CC1-FHA dimer is essential for KIF1A-mediated axonal transport of synaptic vesicles in C. elegans. *Biochem. Biophys. Res. Commun.* **435**, 441–446 (2013).
52. Richmond, J.E. & Jorgensen, E.M. One GABA and two acetylcholine receptors function at the *C. elegans* neuromuscular junction. *Nat. Neurosci.* **2**, 791–797 (1999).
53. Kang, L., Gao, J., Schafer, W.R., Xie, Z. & Xu, X.Z. *C. elegans* TRP family protein TRP-4 is a pore-forming subunit of a native mechanotransduction channel. *Neuron* **67**, 381–391 (2010).
54. Liewald, J.F. *et al.* Optogenetic analysis of synaptic function. *Nat. Methods* **5**, 895–902 (2008).

doi:10.1038/nsmb.3038